Check for updates

ChemPhysChem

Research Article
doi.org/10.1002/cphc.202500196

Chemistry Europe
European Chemical Societies Publishing

www.chemphyschem.org

Exploring the Photophysical Processes of an Al^{3+} Sensor Based on Schiff Base

Bingqing Sun, Haoyang Song, Yi Nan, Lei Liu,* and Juyoung Yoon*

Schiff bases are commonly used as building blocks in the development of turn-on sensors for Al^{3+} detection. The isomerization of the C=N bond in Schiff bases is generally believed to induce fluorescence quenching. Inhibiting this isomerization process through interactions with the target ion, Al^{3+}, enhances fluorescence, enabling its detection. This mechanism is widely used to explain turn-on signals in similar sensors. However, the photophysical processes of such sensors may be more complex, necessitating a deeper understanding of their underlying sensing mechanisms. This study presents a comprehensive investigation into the photophysical processes and sensing mechanism of a turn-on sensor for Al^{3+} featuring a Schiff base moiety. Multiple excited-state intramolecular proton transfer (ESIPT) processes are observed, all closely associated with the Schiff base structure. These ESIPT processes trigger C=N isomerization, leading to the formation of two nonemissive twisted intramolecular charge transfer (TICT) states. In addition to C=N isomerization, two bond rotation processes with lower energy barriers are identified. These rotational processes generate two additional nonemissive TICT states and play a dominant role in the weak fluorescence of the sensor. This elucidation of photophysical processes provides a clearer understanding of the Al^{3+} sensing mechanism.

1. Introduction

Aluminum is one of the most abundant elements in the Earth's crust and plays a crucial role in various industrial sectors, including transportation, packaging, and aerospace.[1] According to a recent report by *Fortune Business Insights*,[2] the global aluminum market was valued at $249.83 billion in 2024 and is projected to reach $403.29 billion by 2032. However, during mining,[3] refining, and product processing, aluminum is inevitably released into the environment in its cationic form, Al^{3+}, leading to severe water and soil contamination. In polluted water, Al^{3+} can precipitate on fish gills, causing osmoregulatory failure.[4] In plants, it inhibits root elongation and reduces crop yields.[5,6] Moreover, excessive Al^{3+} intake in humans has been linked to Alzheimer's disease, prompting the WHO to set an upper limit of 7.4 μM for Al^{3+} concentration in drinking water.[7,8] Therefore, the precise detection of Al^{3+} is of great importance for environmental protection and human health.

Fluorescence sensors based on small organic fluorophores have garnered increasing attention for cation detection.[9–13] Compared to traditional analytical methods, these sensors are typically cost-effective, rapid, and highly customizable. Schiff bases are widely utilized as key building blocks in the design of such sensors. Notably, they provide coordination sites for Al^{3+} recognition; on the other hand, their C=N moiety serves as an effective linker, connecting electron-donating and electron-withdrawing groups to regulate the internal charge transfer (ICT) process.[14,15] It is generally accepted that cis-trans isomerization of the C=N bond can lead to significant fluorescence quenching. Upon coordination with a target cation, such as Al^{3+}, this isomerization is inhibited, resulting in fluorescence enhancement. Consequently, Schiff base-based sensors typically function as turn-on sensors. This mechanism is widely used to explain turn-on fluorescence signals and guide the rational design of similar sensors.[16–18] However, the photophysical process of these sensors is likely more complex, and their weak fluorescence may originate from additional processes beyond C=N isomerization.[19]

A recent study by Lu et al.[20] reports the design and synthesis of a turn-on sensor, QNP ((E)-N′-(5-chloro-2-hydroxybenzylidene) quinoline-2-carbohydrazide), for Al^{3+} detection. As shown in **Scheme 1**, the sensor consists of three components: the quinoline moiety (P1) serves as the fluorophore, the 4-chlorophenol moiety (P2) acts as an electron acceptor, and the Schiff base moiety functions as the conjugate linker. Sensor QNP exhibits minimal fluorescence, which Lu et al. attribute to the combined effects of ICT from P1 to P2 and C=N isomerization. They propose that Al^{3+} coordinates with the sensor, inhibiting both C=N isomerization and the ICT process, thereby triggering fluorescence and enabling Al^{3+} detection. However, their study does not provide direct evidence to support

B. Sun, L. Liu
College of Resource and Environment
Anhui Science and Technology University
Fengyang 233100, China
E-mail: liulei@feipan.org

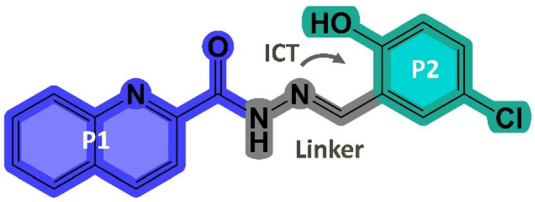
H. Song, Y. Nan, J. Yoon
Department of Chemistry and Nanoscience
Ewha Womans University
Seoul 03760, Republic of Korea
E-mail: jyoon@ewha.ac.kr

H. Song, Y. Nan, J. Yoon
Graduate Program in Innovative Biomaterials Convergence
Ewha Womans University
Seoul 03760, Korea

Supporting information for this article is available on the WWW under https://doi.org/10.1002/cphc.202500196

© 2025 The Author(s). ChemPhysChem published by Wiley-VCH GmbH. This is an open access article under the terms of the Creative Commons Attribution-NonCommercial License, which permits use, distribution and reproduction in any medium, provided the original work is properly cited and is not used for commercial purposes.

© 2025 The Author(s). ChemPhysChem published by Wiley-VCH GmbH



Scheme 1. Structural formula of sensor QNP.

this mechanism. The hydroxyl group on P2 is likely to form multiple hydrogen bonds with the nitrogen atom of the linker and the oxygen atom of P2. These hydrogen bonds could induce excited-state intramolecular proton transfer (ESIPT) processes, which would influence the fluorescence properties of the sensor.[7,21–29] Additionally, the N—N and C—N bonds surrounding the Schiff base may undergo rotational motion in the excited state, potentially leading to nonemissive states. Thus, the actual excited-state dynamics of sensor QNP are likely more complex than previously suggested. A detailed investigation into the photophysical processes of the sensor and Al^{3+} sensing mechanism is essential for a more accurate understanding of its fluorescence behavior.

Building on these considerations, this study conducts a series of theoretical investigations into the excited-state dynamics of sensor QNP using density functional theory (DFT) and time-dependent density functional theory. By mapping the potential energy surface (PES) of the sensor, two ESIPT processes are identified. Notably, C=N isomerization does not occur until these ESIPT processes take place. Following C=N isomerization, two dark states characteristic of twisted intramolecular charge transfer (TICT) are generated. Additionally, the rotation of the C—C bond adjacent to the C=N bond is observed, leading to the formation of two additional TICT states. The energy barrier for C—C bond rotation is significantly lower than that of C=N isomerization, suggesting that excited-state C—C bond rotation plays a dominant role in fluorescence quenching rather than C=N isomerization. After clarifying the photophysical processes of the sensor, the Al^{3+} sensing mechanism is further examined from multiple perspectives, offering valuable insights for the rational design of similar sensors.

2. Results and Discussions

2.1. Excitation Process of the Sensor

Ground state optimized structure of QNP (S_0-1) is shown in **Figure 1**. As shown in Figure 1a and **Table 1**, the sensor adopts a planar structure, with all four dihedrals (D1–D4) measuring 0°. Independent gradient model (IGM) analysis (Figure S1a, Supporting Information) on the sensor is performed to give an overall view of the intramolecular interactions. According to IGM theory, the blue surface indicates a strong interaction. Herein, a comparatively strong hydrogen bond, with a bond length of 1.70 Å, is observed between N3 and H1. To evaluate the possibility of a ground-state intramolecular proton transfer process, a series of relaxed scans along the proton transfer coordinate is performed. As is shown in Figure S1b, Supporting Information, the energy keeps rising as the H1 approaches N3. No stable structures are located, indicating that S_0-1 represents the most stable structure in the ground state. For convenience, the energy of S_0-1 is set to 0 kJ mol^{-1}.

The excitation process of QNP is analyzed by calculating excitation energies based on its ground-state structure. As shown in **Table 2**, photoexcitation primarily populates the sensor into the S_1 state, as the $S_0 \rightarrow S_1$ transition exhibits the highest oscillator strength (0.585). The excitation energy is calculated to be 354 nm, which is in agreement with the experimentally reported absorption peak at 342 nm. This agreement validates the theoretical approach used in this study. Since the $S_0 \rightarrow S_1$ excitation involves a highest occupied molecular orbital (HOMO) → lowest unoccupied molecular orbital (LUMO) transition, the corresponding molecular orbitals are plotted in Figure 1 to provide insight into the ICT characteristics of the sensor. The HOMO is primarily localized on the P2 moiety and the linker, while the LUMO is mainly distributed across the P1 moiety and the linker. This indicates a clear ICT transition from P2 to P1, contradicting Lu et al.'s assumption that ICT occurs from P1 to P2. Electron-hole analysis is performed to verify this ICT feature further.[30] As shown in Figure 1d, an equivalent of 0.50 electrons is transferred from P2 to P1, with a spatial separation of 5.24 Å between the electron and hole. These findings confirm that the originally proposed ICT direction is not right.

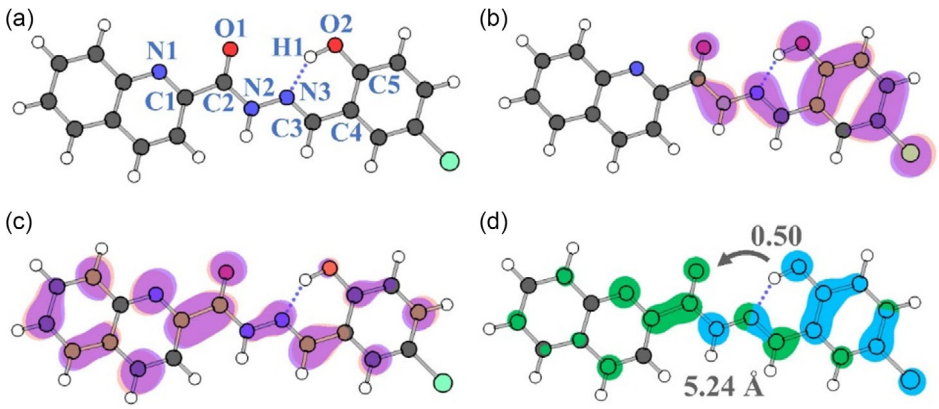


Figure 1. a) Optimized ground-state structure of QNP (S_0-1); b) HOMO of S_0-1; c) LUMO of S_0-1; d) electron-hole distribution after $S_0 \rightarrow S_1$ excitation (isosurface in cyan represents the distribution of hole, isosurface in green represents the distribution of electron).

© 2025 The Author(s). ChemPhysChem published by Wiley-VCH GmbH

14397641, 2025, 17, Downloaded from https://chemistry-europe.onlinelibrary.wiley.com/doi/10.1002/cphc.202500196 by Ewha Womans University Library, Wiley Online Library on [13/01/2026]. See the Terms and Conditions (https://onlinelibrary.wiley.com/terms-and-conditions) on Wiley Online Library for rules of use; OA articles are governed by the applicable Creative Commons License

14397641, 2025, 17, Downloaded from https://chemistry-europe.onlinelibrary.wiley.com/doi/10.1002/cphc.202500196 by Ewha Womans University Library, Wiley Online Library on [13/01/2026]. See the Terms and Conditions (https://onlinelibrary.wiley.com/terms-and-conditions) on Wiley Online Library for rules of use; OA articles are governed by the applicable Creative Commons License

Table 1. Geometrical information of local minima and saddle points of the sensor (D1 represents dihedral N1C1C2N2, D2 represents dihedral C1C2N2N3, D3 represents dihedral C2N2N3C3, and D4 represents dihedral N2N3C3C4).

	O1-H1	O2-H1	N3-H1	D1	D2	D3	D4
S_0-1	2.97 Å	0.99 Å	1.70 Å	0°	0°	0°	0°
S_1-1	2.68 Å	1.01 Å	1.64 Å	0°	0°	0°	0°
S_1-2	2.15 Å	1.83 Å	1.04 Å	0°	0°	0°	0°
S_1-3	0.99 Å	2.69 Å	1.82 Å	1°	1°	8°	1°
TICT-1	2.26 Å	2.72 Å	1.02 Å	47°	6°	3°	86°
TICT-2	2.82 Å	3.65 Å	1.01 Å	−40°	0°	73°	19°
TICT-3	0.99 Å	3.05 Å	1.86 Å	6°	0°	−2°	80°
TICT-4	0.98 Å	4.50 Å	1.93 Å	3°	2°	1°	0°
TS1	2.44 Å	1.22 Å	1.27 Å	0°	0°	0°	0°
TS2	1.28 Å	2.28 Å	1.25 Å	1°	−6°	8°	0°
TS3	2.20 Å	2.65 Å	1.02 Å	30°	3°	32°	43°
TS4	0.99 Å	2.89 Å	1.84 Å	2°	−1°	3°	59°
TS5	2.10 Å	2.45 Å	1.17 Å	19°	−2°	5°	1°
TS6	0.99 Å	3.03 Å	1.86 Å	3°	2°	12°	0°

2.2. ESIPT Process of the Sensor

Upon excitation, the electron distribution across the sensor undergoes significant changes, potentially triggering multiple dynamic processes on the S_1 state PES. To investigate these processes, the S_1 state structure of the sensor (S_1-1) is optimized using S_0-1 as the initial geometry. As shown in Table 1, the planar structure is maintained in the S_1 state. Deactivation from S_1-1 corresponds to the L → H transition. Electron-hole analysis (**Figure 2**a) reveals that 0.63 electrons are transferred from P1 to P2 and the linker. The oscillator strength for this transition is high (0.881), suggesting that S_1-1 should be highly emissive. However, no fluorescence was observed in the original experiment, indicating the presence of nonemissive decay on the S_1 PES. A closer examination of the S_1-1 structure reveals that the hydrogen bond between N3 and H1 shortens to 1.64 Å, strengthening the interaction. This enhanced hydrogen bonding likely facilitates an ESIPT process, which could significantly influence the photophysical behavior of the sensor. As shown in **Figure 3**, an ESIPT from O2 to N3 is identified, with a transition state (TS1) located along this pathway. The associated energy barrier is only 10.7 kJ/mol, leading to the formation of a more stable structure, S_1-2. The ESIPT rate constant is calculated using Equation (1) and (2);[31,32]

$$k = \kappa \frac{k_B T}{h} e^{-\Delta G/RT} \tag{1}$$

$$\kappa = 1 + \frac{1}{24}\left[\frac{h I_m(V^{\neq})}{k_B T}\right]^2 \tag{2}$$

where h represents the Planck constant, κ is the transmission coefficient, and $I_m(V^{\neq})$ denotes the transition state imaginary frequency. The rate constant is determined to be $7.26 \times 10^{11}\ S^{-1}$. This rapid transition suggests that the sensor quickly relaxes to S_1-2 after photoexcitation. Deactivation of S_1-2 (Table 2) still corresponds to the L → H transition, with an electron-hole distribution similar to S_1-1. The oscillator strength remains high (0.529), indicating that this state is also emissive. To further investigate potential nonemissive pathways, additional exploration of the S_1 PES is conducted. Notably, following the first ESIPT process, a new hydrogen bond forms between O1 and H1 with a bond length of 2.15 Å. This interaction suggests the possibility of a second ESIPT, where proton transfer occurs from N3 to O1. A detailed PES scan confirms the presence of a stable ESIPT product (S_1-3) and the corresponding transition state (TS2). As shown in Figure 3, the second ESIPT process encounters a higher energy barrier (34.6 kJ mol^{-1}) compared to the first. Despite this, the calculated rate constant remains relatively high ($5.11 \times 10^8\ s^{-1}$), suggesting that S_1-2 and S_1-3 likely coexist. Deactivation of S_1-3, as presented in Table 2, also exhibits a high oscillator strength (0.599), confirming its emissive nature. Given that all identified ESIPT products remain emissive, additional investigation into nonemissive decay pathways on the S_1 PES is necessary.

2.3. TICT States on the S_1 State PES

C═N isomerization on the excited-state PES is often considered a key factor in fluorescence quenching in sensors. To determine whether this process occurs in sensor QNP, the behavior of S_1-1 (cis-structure) is examined in greater detail. As is shown in Figure S2h, Supporting Information, the C═N bond is manually twisted by setting the dihedral angle D4 to 90°, which serves as the initial guess for optimizing the trans-structure. However, no stable structure is located, indicating that isomerization of the C═N bond in S_1-1 is not likely to happen. This finding contradicts the assumption made by Lu et al.[20] that C═N isomerization is responsible for weak fluorescence. As established in Section 3.2, S1-2 and S1-3 are comparatively more stable than S_1-1, suggesting that nonemissive pathways are more likely associated with these two minima. To further explore this, the C═N isomerization of S_1-2 is investigated by setting dihedral D4 to 90° as the initial guess for optimization. Unlike in S_1-1, a stable trans-structure of S_1-2 is successfully located and designated as TICT-1. As shown in Figure S2d, Supporting Information, and Table 1, the dihedral angle D4 in

© 2025 The Author(s). ChemPhysChem published by Wiley-VCH GmbH

Table 2. Excitation and deactivation energies of the sensor were calculated at the PBE0 functional and CAM-B3LYP functional. The absorption peaks obtained from the experiment are given in parentheses (H represents HOMO, L represents LUMO, and f is oscillator strength).

	Contribution	Energy (nm)	f
PBE0			
S_0-1			
$S_0 \rightarrow S_1$	H → L (98%)	354 (342)	0.585
$S_0 \rightarrow S_2$	H-1 → L (87%)	308	0.025
S_1-1			
$S_1 \rightarrow S_0$	L → H (98%)	450	0.881
S_1-2			
$S_1 \rightarrow S_0$	L → H (98%)	516	0.529
S_1-3			
$S_1 \rightarrow S_0$	L → H (98%)	767	0.599
TICT-1			
$S_1 \rightarrow S_0$	L → H (98%)	2554	0.000
TICT-2			
$S_1 \rightarrow S_0$	L → H (98%)	2009	0.000
TICT-3			
$S_1 \rightarrow S_0$	L → H (98%)	1399	0.001
TICT-4			
$S_1 \rightarrow S_0$	L → H (98%)	1433	0.000
CAM-B3LYP			
S_0-1			
$S_0 \rightarrow S_1$	H → L (65%)	305 (342)	0.781
$S_0 \rightarrow S_2$	H-1 → L (64%)	278	0.030
S_1-1			
$S_1 \rightarrow S_0$	L → H (83%)	385	1.145
S_1-2			
$S_1 \rightarrow S_0$	L → H (81%)	445	0.524
S_1-3			
$S_1 \rightarrow S_0$	L → H (89%)	565	1.011
TICT-1			
$S_1 \rightarrow S_0$	L → H (94%)	1369	0.000
TICT-2			
$S_1 \rightarrow S_0$	L → H (96%)	1120	0.000
TICT-3			
$S_1 \rightarrow S_0$	L → H (93%)	1055	0.001
TICT-4			
$S_1 \rightarrow S_0$	L → H (92%)	648	0.000

TICT-1 is 86°, indicating a highly twisted structure. The deactivation process from TICT-1 corresponds to an L→H transition with an oscillator strength of only 0.000. The electron-hole distribution (**Figure 5**a) reveals that 0.48 electrons transfer from P2 to the linker, confirming that TICT-1 is a nonemissive TICT state. The transition state for the C═N isomerization (TS3) is then identified, with an associated energy barrier of 40.4 kJ mol^{-1} (**Figure 4**). The rate constant for this isomerization is calculated to be 4.93×10^7 s^{-1}, significantly slower than the two ESIPT processes. Consequently, this process is not competitive with ESIPT and is unlikely to occur. To further verify this conclusion, the emission rate constant of S_1-2 is calculated using Equation (3):[33]

$$k_{flu} = \frac{2f\Delta E^2}{3} \quad (3)$$

where f is the oscillator strength and ΔE is the deactivation energy in cm^{-1}. The emission rate constant is determined to be 1.33×10^8 s^{-1}, significantly larger than the isomerization rate constant. This confirms that the C═N isomerization from S_1-2 is improbable and has minimal influence on the fluorescence properties of the sensor. A similar analysis is conducted for S_1-3. As shown in Figure 4, a stable trans-structure of S_1-3, TICT-3, is identified. However, the energy of TICT-3 is significantly higher than that of S_1-3. These findings indicate that C═N isomerization from S_1-3 is not feasible. Based on these analyses, C═N isomerization in sensor QNP is unlikely to occur, contradicting the mechanism proposed by Lu et al. The true mechanism underlying the fluorescence behavior of the sensor requires further investigation.

Notably, the adjacent C—C single bond (C3—C4) near the C═N bond is rotatable, potentially leading to the formation of TICT states. To investigate this, the C3—C4 bond of S_1-2 is manually rotated by 90° as an initial guess for optimization. This process successfully yields a local minimum with a twisted structure, designated as TICT-2 (Table 1, Figure S2e, Supporting Information). As shown in Figure 4, TICT-2 is 15.2 kJ mol^{-1} lower in energy than S_1-2, indicating that it is more thermodynamically stable. A transition state (TS5) is identified along the rotation coordinate, with an energy barrier of just 13.4 kJ mol. The rate constant for this rotation is calculated to be 2.79×10^{10} s^{-1}, significantly faster than that of C═N isomerization. This suggests that the rotation process is both thermodynamically and kinetically favorable. As shown in Table 2, the deactivation corresponds to the L→H transition, with an oscillator strength close to zero. The electron-hole distribution (Figure 5b) reveals that ≈0.77 electrons transfer from the linker to P2. The highly twisted structure, near-zero oscillator strength, and pronounced ICT characteristics confirm that TICT-2 is a typical nonemissive TICT state. Given that the rate of C3—C4 rotation is considerably higher than the emission rate of S_1-2, TICT-2 is likely responsible for quenching the fluorescence of the sensor, making it the dominant factor contributing to the weak fluorescence observed. Since S_1-3 is also a

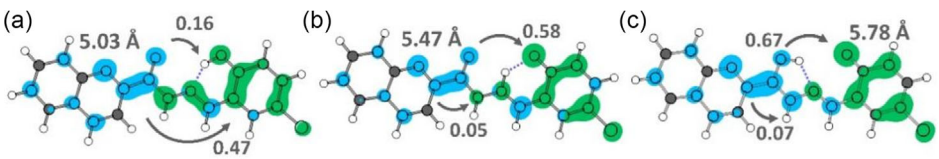


Figure 2. Electron-hole distribution for the deactivation of a) S_1-1, b) S_1-2, and c) S_1-3.

© 2025 The Author(s). ChemPhysChem published by Wiley-VCH GmbH

14397641, 2025, 17, Downloaded from https://chemistry-europe.onlinelibrary.wiley.com/doi/10.1002/cphc.202500196 by Ewha Womans University Library, Wiley Online Library on [13/01/2026]. See the Terms and Conditions (https://onlinelibrary.wiley.com/terms-and-conditions) on Wiley Online Library for rules of use; OA articles are governed by the applicable Creative Commons License

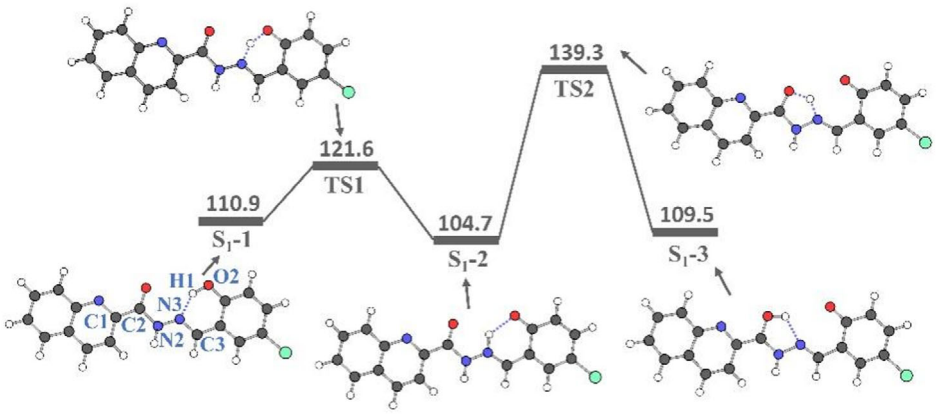


Figure 3. Local minima and transition states for ESIPT processes.

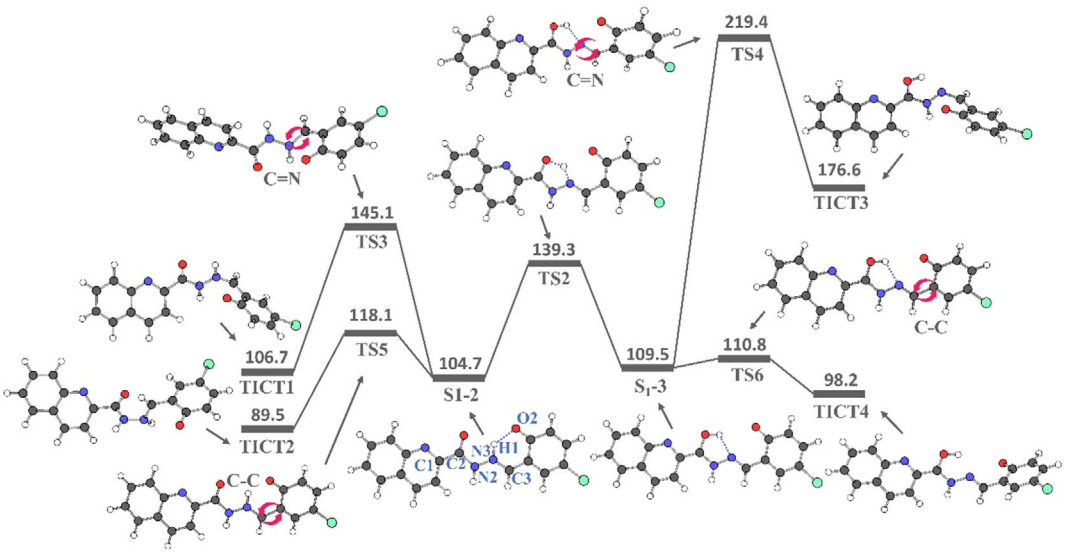


Figure 4. Local minima and transition states for bond-rotating processes.

possible local minimum, the effect of C3—C4 rotation from this state is further explored. As shown in Table 1 and Figure S2g, Supporting Information, another twisted rotamer, TICT-4, is identified. Similar to the case of S_1-2, this rotational process is both thermodynamically and kinetically favorable (Figure 4). The oscillator strength of the deactivation from TICT-4 is also close to zero, and the state exhibits strong ICT characteristics (Table 2, Figure 5), confirming that it is another nonemissive dark state. However, given that the energy barrier from S_1-2 to S_1-3 is relatively high and S_1-2 is more stable, TICT-4 is less competitive than TICT-2 and likely serves as a secondary nonemissive pathway. Additionally, potential nonemissive rotamers from the rotation of other bonds, including C1—C2, C2—N2, and N2—N3, are also explored. However, no stable structures are identified for these rotations. As the sensor has a clear ICT feature, the range-separated functional CAM-B3LYP is chosen to recalculate the excitation and deactivation processes of the sensor to validate the PBE0 functional. The excitation and deactivation energies of the sensor calculated with CAM-B3LYP-D3/TZVP are listed in Table 2. Both functionals output similar results, as the oscillator strength and molecular orbitals involved in the excitation processes are quite close. Molecular orbitals are then plotted in Figure S5 and Figure S6, Supporting Information. As shown, the molecular orbitals in Figure S5, Supporting Information, is

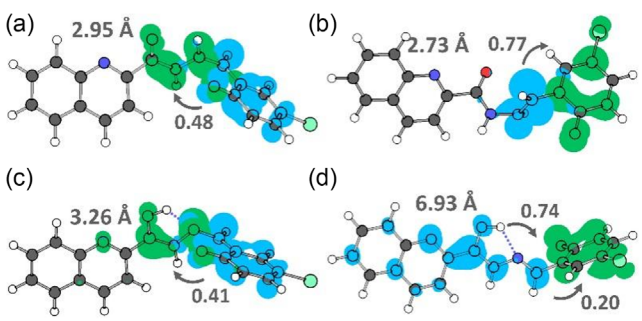


Figure 5. Electron-hole distribution for the deactivation of a) TICT-1, b) TICT-2, c) TICT-3, and d) TICT-4.

© 2025 The Author(s). ChemPhysChem published by Wiley-VCH GmbH

14397641, 2025, 17, Downloaded from https://chemistry-europe.onlinelibrary.wiley.com/doi/10.1002/cphc.202500196 by Ewha Womans University Library, Wiley Online Library on [13/01/2026]. See the Terms and Conditions (https://onlinelibrary.wiley.com/terms-and-conditions) on Wiley Online Library for rules of use; OA articles are governed by the applicable Creative Commons License

quite similar to that in Figure S3, Supporting Information. Also, the orbitals in Figure S6, Supporting Information, are quite similar to that in Figure S4, Supporting Information. Herein, both functionals can predict the ICT feature of the sensor.

As all the above TICT states hold highly twisted structures, the minimum energy conical intersection (MECI) between the S_0 and S_1 state PES may also result in fluorescence quenching. This issue is further explored by using the linearly interpolated internal coordinate (LIIC). Taking TICT-1 as an example, 8 structures are interpolated between S_1-2 and TICT-1. The self consistent field (SCF) energy of the 10 structures (including S_1-2 and TICT-1) in S_0 and S_1 states is calculated and shown in **Figure 6**. The TICT-1 structure has a low energy on the S_1 state PES while a high energy on the S_0 state PES, indicating a possible intersection. Herein, the MECI points are close to the TICT states, which may also contribute to the weak fluorescence of the sensor.

2.4. Al^{3+} Sensing Mechanism

With a comprehensive understanding of the excited-state dynamics of the sensor, the sensing mechanism for Al^{3+} is investigated. To identify potential binding sites, the electrostatic potential surface (EPS) is generated, revealing red and yellow zones around O1 and O2, indicating that Al^{3+} is likely to be attracted to these regions due to electrostatic forces (**Figure 7**a). While the EPS analysis can give a direct view of the potential site for electrostatic interaction, the reactivity of the site of a certain molecule can be reflected by the Fukui function.[34] The larger the Fukui function value is, the more reactive the site will be. Next, the Fukui function f- is calculated, and its distribution is plotted in Figure 7b. Among all sites, O2 exhibits the highest f-value, making it the most favorable center for nucleophilic attack. As proposed by Lu et al, the hydroxyl hydrogen is deprotonated, and the Al^{3+} binds to two chloride ions and one water molecule, which makes the complex neutral. Herein, by placing this coordinated Al^{3+} close to O2, a stable analyte-sensor complex (QNP-Al-S_0) is obtained after geometry optimization. This complex adopts a 6-coordinated structure (Figure 7, Table S1, Supporting Information), with three coordination bonds forming between Al^{3+} and the sensor. Additionally, charge decomposition analysis (CDA) is performed to further investigate the electronic interaction between the analyte and the sensor. As shown in Table S2, Supporting Information, and **Figure 8**, 0.77 electrons transfer from the sensor to Al^{3+} upon coordination. Among all molecular orbitals, H-11 contributes the most (0.06 electrons) to this charge transfer process, accompanied by a strong back donation (0.03 electrons), making it an ideal candidate for electronic coupling analysis. The molecular orbital (MO) composition of the complex is then examined by decomposing it into fragment

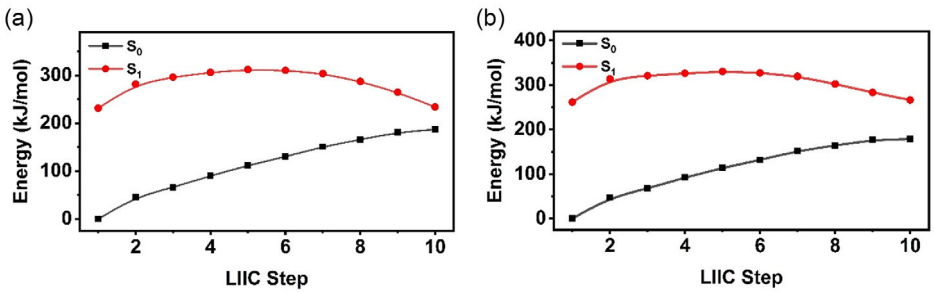


Figure 6. LIIC Energy curves from S_1-2 structure (step 1) to TICT-1 structure (step 10) on the ground state and a) excited state obtained via PBE0 and b) CAM-B3LYP.

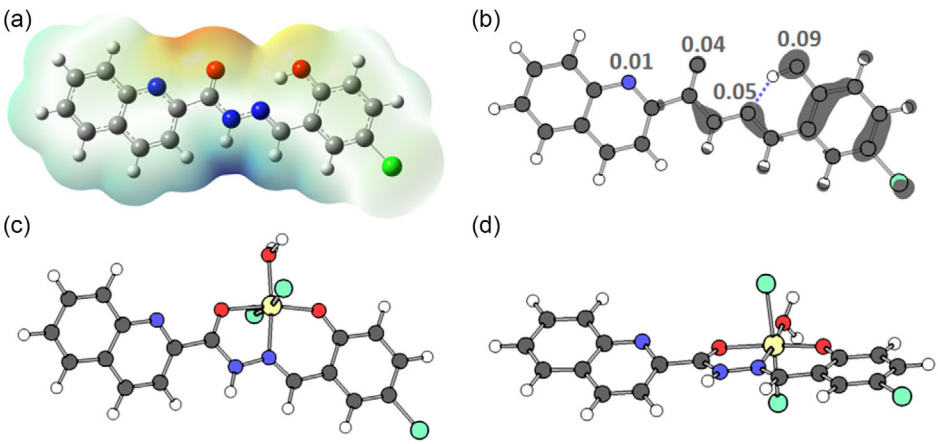


Figure 7. a) EPS of the sensor in the ground state; b) isosurface of Fukui function f-; c) optimized ground-state structure of the analyte-sensor complex QNP-Al-S_0 (top view); d) optimized ground-state structure of QNP-Al-S_0 (side view).

© 2025 The Author(s). ChemPhysChem published by Wiley-VCH GmbH

14397641, 2025, 17, Downloaded from https://chemistry-europe.onlinelibrary.wiley.com/doi/10.1002/cphc.202500196 by Ewha Womans University Library, Wiley Online Library on [13/01/2026]. See the Terms and Conditions (https://onlinelibrary.wiley.com/terms-and-conditions) on Wiley Online Library for rules of use; OA articles are governed by the applicable Creative Commons License

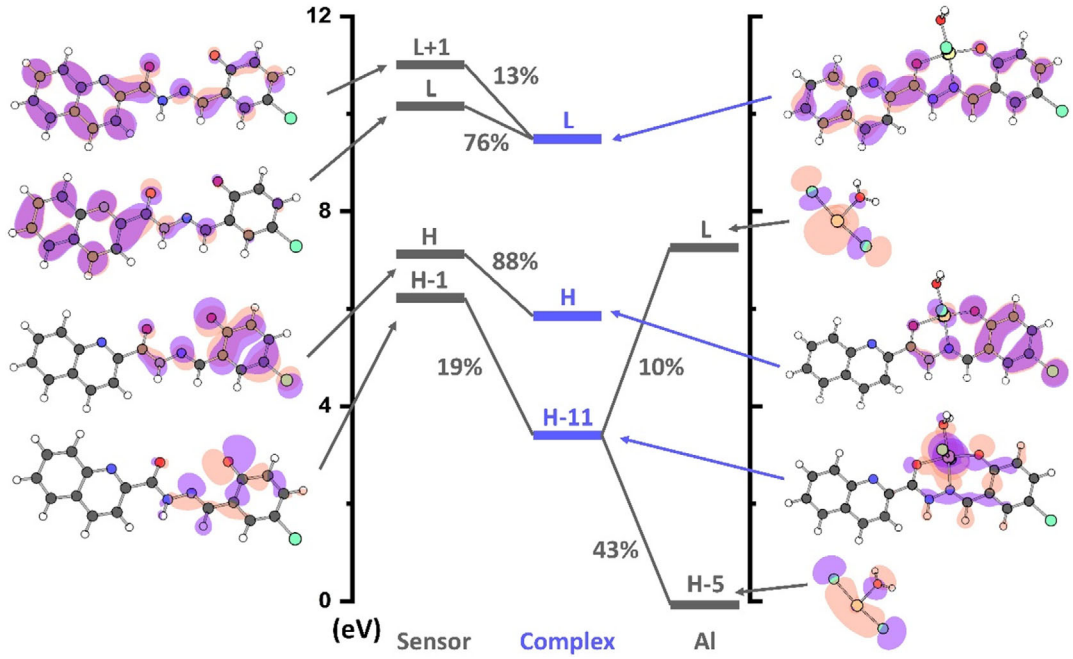


Figure 8. The orbital interaction diagram for QNP-Al-S_0.

Table 3. Excitation and deactivation energies of the analyte-sensor complex.

	Contribution	Energy (nm)	f
QNP-Al-S_0			
$S_0 \rightarrow S_1$	H → L (98%)	420	0.294
$S_0 \rightarrow S_1$	H-1 → L (72%)	329	0.032
QNP-Al-S_1			
$S_1 \rightarrow S_0$	H → L (98%)	546	0.445

orbitals (FO) from both the sensor and Al^{3+}. Specifically, MO H-11 originates from FO H-1 (19%) of the sensor, FO H-5 (43%) of Al^{3+}, and FO L (10%) of Al^{3+}. This confirms that the observed 0.06-electron transfer occurs through the interaction of FO H-1 of the sensor and FO L of Al^{3+}. Given the significant total charge transfer (0.77 electrons), strong electronic coupling between the sensor and analyte is expected. The bond energy of the three coordination bonds is then calculated using the SCF energy difference between the complex and the isolated sensor and Al^{3+} at the PBE0/def2TZVP level of theory. The result is −717.4 kJ mol^{-1}, indicating strong coordination. These robust coordination bonds effectively lock the molecule conformation, preventing the rotation of the C3—C4 single bond. Consequently, the fluorescence of the sensor is restored, leading to a fluorescence "turn-on" response.

The photophysical process of the analyte-sensor complex is then investigated to validate the Al^{3+} sensing mechanism. As shown in **Table 3**, the dominant excitation corresponds to the

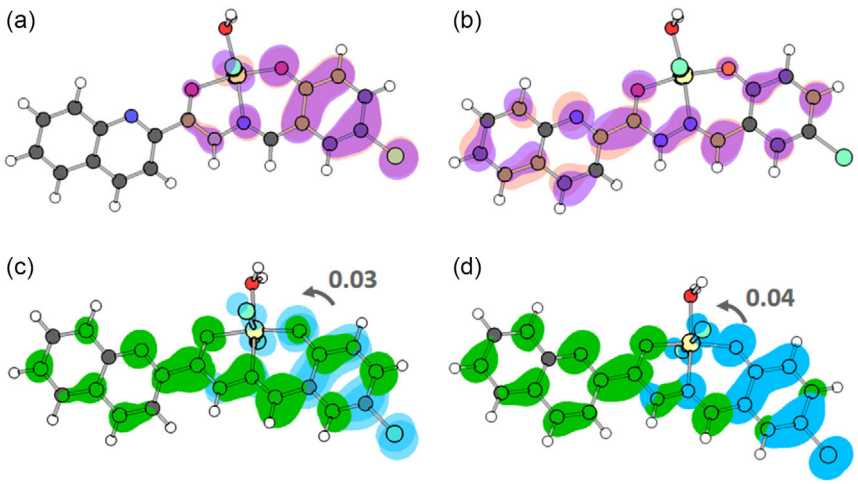


Figure 9. a) HOMO of QNP-Al-S_0; b) LUMO of QNP-Al-S_0; c) electron-hole distribution of $S_0 \rightarrow S_1$ excitation of QNP-Al-S_0; d) electron-hole distribution of $S_0 \rightarrow S_1$ excitation of QNP-Al-S_1.

© 2025 The Author(s). ChemPhysChem published by Wiley-VCH GmbH

1439764l, 2025, 17, Downloaded from https://chemistry-europe.onlinelibrary.wiley.com/doi/10.1002/cphc.202500196 by Ewha Womans University Library, Wiley Online Library on [13/01/2026]. See the Terms and Conditions (https://onlinelibrary.wiley.com/terms-and-conditions) on Wiley Online Library for rules of use; OA articles are governed by the applicable Creative Commons License

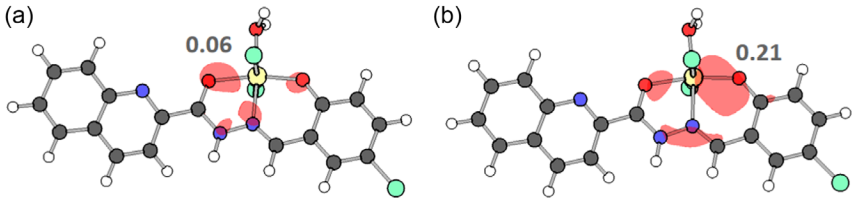


Figure 10. Overlap zones and overlap values between a) LUMO of the sensor fragment and LUMO of the Al^{3+} fragment, and b) HOMO-1 of the sensor fragment and LUMO of the Al^{3+} fragment.

$S_0 \rightarrow S_1$ transition, which exhibits the largest oscillator strength. The excitation energy is calculated to be 420 nm, closely matching the experimental value of 401 nm. This transition involves the H→L orbital transition, with the corresponding molecular orbitals visualized in **Figure 9**. No intermolecular electron transfer from the sensor to Al^{3+} is observed, which is further confirmed by the electron-hole distribution analysis (Figure 9c). Electron-hole analysis of the S_1 state (Figure 9 d) indicates that this state also has no intermolecular electron transfer feature. The optimized S_1 structure (Table S1, Supporting Information) is then obtained, and its deactivation process is analyzed and shown in Table 3. The emission process exhibits a large oscillator strength. These findings confirm that the analyte-sensor complex is highly emissive, clearly validating the Al^{3+} sensing mechanism.

Notably, both the S_1 and S_2 states are locally excited states, with no significant charge transfer occurring from the sensor to Al^{3+}.[35] Typically, this phenomenon is attributed to the LUMO of the donor being lower in energy than the LUMO of the acceptor.[36] However, in this case, the LUMO energy of the sensor is higher than the LUMO of Al^{3+} (Figure 8). While a positive energy gap may promote electron transfer from the donor to the acceptor, orbital overlap also plays a crucial role in determining electron transfer efficiency.[37,38] To further examine this, the orbital overlap between the LUMO of the sensor and the LUMO of Al^{3+} is calculated, and the overlapping region is visualized in **Figure 10**a. As shown, the overlap is primarily localized around the O1 site and is relatively small, with an overlap value of just 0.06. In contrast, the overlap between H-1 of the sensor and L of Al^{3+} (Figure 10b), which facilitates electron transfer during coordination bond formation, is significantly larger. Therefore, the minimal overlap between the LUMO of the sensor and the LUMO of Al^{3+} is insufficient to promote electron transfer during the excitation process.

3. Conclusion

In conclusion, the photophysical processes of the sensor QNP have been thoroughly investigated. The S_1 state PES reveals two ESIPT processes, two C═N isomerization processes, and two bond rotation processes. Transition states, energy barriers, and rate constants for these pathways have been determined and compared to assess their likelihood. The findings demonstrate that the weak fluorescence of the sensor originates from the rotation of the C—C bond adjacent to the C═N bond, which exhibits a lower energy barrier and a faster reaction rate. This refutes the widely accepted notion that C═N isomerization is responsible for fluorescence quenching. Building on this understanding of the photophysical behavior of the sensor, the Al^{3+} detection mechanism is explored. Strong electronic coupling between the sensor and Al^{3+} is observed, leading to the formation of strong coordination bonds. These bonds effectively restrict the rotational motion of the C—C bond, thereby restoring the fluorescence of the sensor. This study provides valuable insights into the design of Al^{3+} sensors and their fluorescence-based detection mechanisms.

4. Experimental Section

Unless otherwise specified, all calculations were performed using the PBE0 function[39] and TZVP basis sets with the Gaussian 16 software package.[40] DFT-D3 dispersion correction was applied throughout the calculations.[41] Since the original experiment by Lu et al. was conducted in DMF, solvation effects were accounted for using the SMD model with DMF as the solvent.[42] All local minima are verified by the absence of imaginary frequencies, while all transition states were confirmed through IRC calculations. CDA, orbital overlap analysis, IGM analysis,[43,44] and Fukui function calculations were performed using Multiwfn 3.8.[45] Charge transfer feature during the photophysical process can be quantified by various methods as described by Ciofini[46] and Lu.[30] In this article, electron-hole analysis[30] was chosen to give a quantified evaluation of the charge-transfer character with the aid of Multiwfn 3.8.[45] All kinetic data were computed at 298 K and 100 kPa. Benchmark studies with CAM-B3LYP functional were provided in the supporting information.

Acknowledgements

This research was supported by the Natural Science Foundation of the Anhui Higher Education Institutions of China (grant no. gxgwfx2021037, grant no. gxgwfx2022027), Foundation of the Anhui Science and Technology University (grant no. 2021zrzd15). J.Y. thanks the National Research Foundation of Korea for the grant funded by the Korean government (MSIT) (2022R1A2C3005420).

Conflict of Interest

The authors declare no conflict of interest.

Data Availability Statement

The data that support the findings of this study are available in the supplementary material of this article.

© 2025 The Author(s). ChemPhysChem published by Wiley-VCH GmbH

14397641, 2025, 17, Downloaded from https://chemistry-europe.onlinelibrary.wiley.com/doi/10.1002/cphc.202500196 by Ewha Womans University Library, Wiley Online Library on [13/01/2026]. See the Terms and Conditions (https://onlinelibrary.wiley.com/terms-and-conditions) on Wiley Online Library for rules of use; OA articles are governed by the applicable Creative Commons License

Keywords: excited-state intramolecular proton transfers · Schiff base · twisted intramolecular charge transfers · turn-on sensors

[1] J. R. Davis, Corrosion of Aluminum and Aluminum Alloys **1999**, ASM International, ISBN 978-1-61503-238-9.
[2] Fortune Business Insights, Aluminum Market Size, Share & Industry Analysis **2025**, https://www.fortunebusinessinsights.com/industry-reports/aluminium-market-100233.
[3] B.O. Rosseland, T. D. Eldhuset, M. Staurnes, *Environ. Geochem. Hlth.* **1990**, *12*, 17.
[4] J. P. Baker, C. L. Schofield, *Water. Air. Soil. Poll.* **1982**, *18*, 289.
[5] S. J. Zheng, J. L. Yang, *Biol. Plant.* **2005**, *49*, 321.
[6] J. Liu, M. A. Piñeros, L. V. Kochian, *J. Integr. Plant Biol.* **2014**, *56*, 221.
[7] Y. Chen, Y. R. Lee, W. Wang, Y. Fang, S. Lu, J. Han, X. Chen, M. H. Kim, J. Yoon, *Angew. Chem. Int. Ed.* **2023**, *62*, e202301765.
[8] M. Hollósi, Z. M. Shen, A. Perczel, G. D. Fasman, *Proc. Natl. Acad. Sci. U S A.* **1994**, *91*, 4902.
[9] S. H. Park, N. Kwon, J. H Lee, J. Yoon, I. Shin, S. Heng, *Chem. Soc. Rev.* **2020**, *49*, 143.
[10] Y. Chen, S. Zheng, M. H. Kim, X. Chen, J. Yoon, *Curr. Opin. Chem. Biol.* **2023**, *75*, 102321.
[11] Y. Zhou, X. Yang, W. J. Jang, M. Yan, J. Yoon, *Coord. Chem. Rev.* **2025**, *522*, 216201.
[12] S. Liu, L. Zhang, H. Kim, J. Sun, J. Yoon, *Coord. Chem. Rev.* **2024**, *501*, 215575.
[13] W. Liu, L. Li, S. Yue, S. Jia, C. Wang, D. Zhang, *Chem. Eur. J.* **2024**, *30*, e202402017.
[14] K. Dev, S. Singh, S. Bhardwaj, P. Kukreti, D. Ramakanth, P. Kumar, S. Saini, P. Roy, V. C. Srivastava, K. Ghosh, P. K. Maji, *Chem. Eur. J.* **2024**, *30*, e202403256.
[15] S. Khan, X. Chen, A. Almahri, E. S. Allehyani, F. A. Alhumaydhi, M. M. Ibrahim, *J. Environ. Chem. Eng.* **2021**, *9*, 106381.
[16] P. Li, R. Li, K. Wang, Q. Liu, B. Ren, Y. Ding, R. Guan, D. Cao, *Spectrochim. Acta. A.* **2022**, *276*, 121213.
[17] H. Xu, W. Chen, L. Ju, H. Lu, *Spectrochim. Acta. A.* **2021**, *247*, 119074.
[18] Q. Wu, L. H. Feng, J. B. Chao, Y. Wang, S. Shuang, *Analyst* **2021**, *146*, 4348.
[19] C. Wang, W. Chi, Q. Qiao, D. Tan, Z. Xu, X. Liu, *Chem. Soc. Rev.* **2021**, *50*, 12656.
[20] W. Lu, J. Chen, J. Shi, L. Xu, S. Yang, B. Gao, *J. Biol. Inorg. Chem.* **2021**, *26*, 57.
[21] Y. Chen, S. Lu, S. A. A. Abedi, M. Jeong, H. Li, M. H. Kim, S. Park, X. Liu, J. Yoon, X. Chen, *Angew. Chem. Int. Ed.* **2023**, *62*, e202311543.
[22] A. C. Sedgwick, L. Wu, H. H. Han, S. D. Bull, X. P. He, T. D. James, J. L. Sessler, B. Z. Tang, H. Tian, J. Yoon, *Chem. Soc. Rev.* **2018**, *47*, 8842.
[23] Z. Tang, T. Bai, P. Zhou, *J. Phys. Chem. A.* **2020**, *124*, 6920.
[24] G. Sun, H. Fang, *J. Phys. Chem. A.* **2023**, *127*, 1857.
[25] G. J. Zhao, K. L. Han, *Acc. Chem. Res.* **2012**, *45*, 404.
[26] F. Ji, Z. Wu, M. Wang, *J. Lumin.* **2022**, *248*, 118914.
[27] P. Zhou, K. Han, *Aggregate* **2022**, *3*, e160.
[28] P. W. Zhou, K. L. Han, *Acc. Chem. Res.* **2018**, *51*, 1681.
[29] R. Bag, Y. Sikdar, S. Sahu, M. M. Islam, S. Mandal, S. Goswami, *Chem. Eur. J.* **2023**, *29*, e202203399.
[30] Z. Liu, T. Lu, Q. Chen, *Carbon* **2020**, *165*, 461.
[31] H. Eyring, *Chem. Rev.* **1935**, *17*, 65.
[32] S. Canneaux, F. Bohr, E. Henon, *J. Comput. Chem.* **2014**, *35*, 82.
[33] R. Chidthong, S. Hannongbua, *J. Comput. Chem.* **2009**, *31*, 1450.
[34] R. G. Parr, W. Yang, *J. Am. Chem. Soc.* **1984**, *106*, 4049.
[35] T. Lu, W. F. Chen, *J. Comput. Chem.* **2012**, *33*, 580.
[36] M. Baharfar, A. C. Hillier, G. Mao, *Adv. Mater.* **2024**, *36*, 2406083.
[37] L. Liu, B. Sun, R. Ding, Y. Mao, *J. Phys. Chem. A* **2022**, *126*, 230.
[38] L. Liu, B. Sun, R. Ding, Y. Mao, *J. Phys. Chem. A* **2021**, *125*, 7867.
[39] C. Adamo, V. Barone, *J. Chem. Phys.* **1999**, *110*, 6158.
[40] M. J. Frisch, G. W. Trucks, H. B. Schlegel, G. E. Scuseria, M. A. Robb, J. R. Cheeseman, G. Scalmani, V. Barone, G. A. Petersson, H. Nakatsuji, X. Li, M. Caricato, A. V. Marenich, J. Bloino, B. G. Janesko, R. Gomperts, B. Mennucci, H. P. Hratchian, J. V. Ortiz, A. F. Izmaylov, J. L. Sonnenberg, D. Williams-Young, F. Ding, F. Lipparini, F. Egidi, J. Goings, B. Peng, A. Petrone, T. Henderson, D. Ranasinghe, et al, *Gaussian 16, Revision A.03*, Gaussian, Inc., Wallingford, CT **2016**.
[41] S. Grimme, J. Antony, S. Ehrlich, H. Krieg, *J. Chem. Phys.* **2010**, *132*, 154104.
[42] A. V. Marenich, C. J. Cramer, D. G. Truhlar, *J. Phys. Chem. B.* **2009**, *113*, 6378.
[43] C. Lefebvre, G. Rubez, H. Khartabil, J. C. Boisson, J. Contreras-García, E. Hénon, *Phys. Chem. Chem. Phys.* **2017**, *19*, 17928.
[44] T. Lu, Q. Chen, *J. Comput. Chem.* **2022**, *43*, 539.
[45] T. Lu, Q. X. Chen, Efficient Simple, *J. Phys. Chem. A* **2023**, *127*, 7023.
[46] C. Adamo, T. L. Bahers, M. Savarese, L. Wilbraham, G. García, R. Fukuda, M. Ehara, N. Rega, I. Ciofini, *Coordin. Chem. Rev.* **2015**, *304*, 166.

Manuscript received: March 14, 2025
Revised manuscript received: June 6, 2025
Version of record online: July 4, 2025

© 2025 The Author(s). ChemPhysChem published by Wiley-VCH GmbH

14397641, 2025, 17, Downloaded from https://chemistry-europe.onlinelibrary.wiley.com/doi/10.1002/cphc.202500196 by Ewha Womans University Library, Wiley Online Library on [13/01/2026]. See the Terms and Conditions (https://onlinelibrary.wiley.com/terms-and-conditions) on Wiley Online Library for rules of use; OA articles are governed by the applicable Creative Commons License